



Title	Collectivity and instability of the $N = Z = 28$ shell gap and strongly deformed bands with $g(9/2)$ configuration in Ni-56
Author(s)	Chiba, Y.; Kimura, M.
Citation	Physical Review C, 89(5), 054313 <a href="https://doi.org/10.1103/PhysRevC.89.054313">https://doi.org/10.1103/PhysRevC.89.054313</a>
Issue Date	2014-05-13
Doc URL	<a href="http://hdl.handle.net/2115/56531">http://hdl.handle.net/2115/56531</a>
Rights	©2014 American Physical Society
Type	article
File Information	PhysRevC_89_054313.pdf



[Instructions for use](#)

# Collectivity and instability of the $N = Z = 28$ shell gap and strongly deformed bands with $g_{9/2}$ configuration in $^{56}\text{Ni}$

Y. Chiba and M. Kimura

*Department of Physics, Hokkaido University, Sapporo 060-0810, Japan*

(Received 24 January 2014; revised manuscript received 10 March 2014; published 13 May 2014)

The positive-parity excited states of  $^{56}\text{Ni}$  and instability of the  $N = Z = 28$  shell gap are discussed on the basis of the antisymmetrized molecular dynamics calculation using the Gogny D1S effective interaction. It is found that  $^{56}\text{Ni}$  is quite soft against oblate deformation and the  $N = Z = 28$  closed-shell configuration amounts to only 62% in the ground state. It is also found that the shell gap easily disappears by prolate deformation, which leads to the coexistence of the almost spherical ground band, excited  $\beta$  and  $\gamma$  bands, and a prolate superdeformed band with  $(f_{7/2})^{-m}(p_{3/2})^m$  configurations within the small excitation energies. Furthermore, in the highly excited region, it is predicted that a couple of strongly deformed bands with  $(sd)^{-m}(pf)^{-n}(g_{9/2})^{m+n}$  configurations are built on the  $0^+$  states around 20 MeV.

DOI: [10.1103/PhysRevC.89.054313](https://doi.org/10.1103/PhysRevC.89.054313)

PACS number(s): 27.40.+z, 21.60.-n, 21.10.Ky, 21.10.Re

## I. INTRODUCTION

In a simple shell-model description, the nucleus  $^{56}\text{Ni}$  is expected to have a doubly closed-shell configuration with the magic number of  $N = Z = 28$ , which is the smallest one generated by the spin-orbit splitting. However, experimental and theoretical studies have revealed that its low-lying and highly excited states manifest very important and interesting aspects of nuclear many-body dynamics.

In the low-lying states of  $^{56}\text{Ni}$ , spherical levels including the ground state and two strongly deformed rotational bands are experimentally known. The first  $2^+$  state which is one of the spherical levels has a relatively small excitation energy of 2.7 MeV [1] and a relatively large value of  $B(E2; 2^+ \rightarrow 0^+) = 112 e^2 \text{fm}^4$  [2–4] compared to other doubly closed-shell nuclei such as  $^{48}\text{Ca}$ , which has the first  $2^+$  state at 3.8 MeV and  $B(E2; 2^+ \rightarrow 0^+) = 17 e^2 \text{fm}^4$ . These observations suggest that  $^{56}\text{Ni}$  is a rather soft double magic nucleus against the collective excitations. Indeed, the Monte Carlo shell-model (MCSM) calculations [5–10] pointed out that the  $f_{7/2}$  closed-shell configuration in the ground state amounts to only 50%–70% and other configurations within the  $pf$  shell play an important role to explain the observed spherical energy levels. Furthermore, they predicted a deformed rotational band built on a  $0^+$  state around 5 MeV, which is dominated by an  $(f_{7/2})^{-4}(p_{3/2})^4$  configuration. Experiments [11–13] have identified this rotational band from the  $2^+$  state at 5.35 MeV up to the  $14^+$  state at 16.35 MeV. Adding to this, another strongly deformed band that is supposed to have negative parity was found and assigned from the  $5^-$  state at 8.89 MeV up to the  $17^-$  state at 19.52 MeV. Based on the mean-field and MCSM calculations [10,11], this band was supposed to have nucleons excited into the upper orbital, the  $g_{9/2}$  shell. These two rotational bands can be regarded as superdeformed (SD) bands owing to their large moment of inertia. Thus, the spherical energy levels indicate the instability of the  $N = Z = 28$  shell closure and the SD bands show the existence of the SD shell gap with  $N = Z = 28$ . Therefore, the detailed study of the low-lying spectrum will provide us important information on the shell structure and instability of the  $N = Z = 28$  magic number in the neutron deficient nuclei.

The highly excited states of  $^{56}\text{Ni}$  or the compound nucleus  $^{56}\text{Ni}^*$  suggest another important aspect of nuclear many-body dynamics. Betts *et al.* [14,15] found intermediate structure resonances with narrow widths in the  $^{28}\text{Si}(^{28}\text{Si}, ^{28}\text{Si}^*)^{28}\text{Si}^*$  reactions at excitation energies of 60 to 70 MeV in a number of exit channels of  $^{28}\text{Si}^* + ^{28}\text{Si}^*$ . Dichter *et al.* [16] also found the similar resonant structures in the measurement of the  $^{40}\text{Ca}(^{16}\text{O}, ^{28}\text{Si}^*)^{28}\text{Si}^*$  reactions. From the analysis of the angular dependence, it was shown that those resonances have the angular momentums ranging from  $L = 36$  to 42. The intermediate resonance structures observed in  $^{28}\text{Si} + ^{28}\text{Si}$  and  $^{40}\text{Ca} + ^{16}\text{O}$  systems are strongly correlated to each other and observed in a number of different exit channels. Therefore, it looks like those reactions proceed through the compound nucleus  $^{56}\text{Ni}^*$ , which is a strongly deformed shape isomeric state [SD or hyperdeformed (HD) states] or dinucleus ( $^{28}\text{Si}^* + ^{28}\text{Si}^*$ ) state.

On the theoretical side, two different approaches have been applied to understand the resonant structure of the compound nucleus  $^{56}\text{Ni}^*$ . (1) Cluster (dinucleus) models [17–21] in which the resonances are regarded to have dinucleus configurations as a result of a potential pocket between two clusters. For example, Uegaki *et al.* [20,21] recently reported their analysis on the resonances of the  $^{28}\text{Si} + ^{28}\text{Si}$  system based on the dinuclear molecular model and successfully explained why the resonant structures are observed in a number of exit channels of  $^{28}\text{Si}^* + ^{28}\text{Si}^*$ . (2) Mean-field models [19,22] which interpret the resonance structure as the strongly deformed shape isomeric state of  $^{56}\text{Ni}^*$  assisted by the strong deformed shell correction. They have reported HD minima in the energy surface, which possibly explains why the same resonant structure appears in both  $^{28}\text{Si} + ^{28}\text{Si}$  and  $^{16}\text{O} + ^{40}\text{Ca}$  channels. Thus, two different approaches explain some aspects of the observed resonant structure. Therefore, we may expect that the resonant structure observed in  $^{56}\text{Ni}^*$  has a dual nature of the cluster and mean-field aspects; i.e., the  $^{56}\text{Ni}$  resonant structure is understood as a strongly deformed isomeric state stabilized by the SD or HD shell effect, but it also has considerable overlap with  $^{28}\text{Si} + ^{28}\text{Si}$  dinuclear configurations, and, hence, it manifests both aspects

of strongly deformed mean field and clustering. We quote similar phenomena reported in the theoretical studies of  $^{12}\text{C} + ^{16}\text{O}$  and  $^{16}\text{O} + ^{16}\text{O}$  molecular resonances [23–25]. For example, in the case of  $^{32}\text{S}$  [23,24], it was shown that the SD state has dual nature of the SD mean field and  $^{16}\text{O} + ^{16}\text{O}$  clustering, which leads to the evolution of the SD states into the  $^{16}\text{O} + ^{16}\text{O}$  molecular bands by the excitation of the intercluster motion. This point of view of “duality” might lead to the unified understanding of the resonant structure of  $^{56}\text{Ni}$ .

In this paper, as a first step of the exploration, we report the results obtained by the antisymmetrized molecular dynamics (AMD) calculation. The aim of the study is twofold. The first is to clarify the properties of the coexisting low-lying states and how the  $N = Z = 28$  shell closure is weakened in  $^{56}\text{Ni}$ . The second is to explore the strongly deformed states at high excitation energies and to examine their relationship with the observed resonant states. In the next section, we briefly explain the theoretical framework of AMD and the methods to analyze the results. In Sec. III, the results are presented. We first discuss the low-lying spectrum. It is shown that  $^{56}\text{Ni}$  is quite soft against the oblate deformation and the  $N = Z = 28$  shell gap easily disappears by prolate deformation, which leads to the coexistence of the almost spherical ground band, excited  $\beta$  and  $\gamma$  bands, and a prolate SD band with  $(f_{7/2})^{-m}(p_{3/2})^m$  configurations at small excitation energies. We then focus on the highly excited states. It is predicted that a couple of strongly deformed bands with  $(sd)^{-m}(pf)^{-n}(g_{9/2})^{m+n}$  configurations are built on the  $0^+$  states around 20 MeV. The final section summarizes this work.

## II. THEORETICAL FRAMEWORK OF ANTISYMMETRIZED MOLECULAR DYNAMICS

The theoretical framework and calculational procedure applied in this study are almost common to those in Ref. [26]. We briefly explain the variational calculation and the generator coordinate method (GCM) which are used to obtain the eigenenergies and the wave functions of the various states of  $^{56}\text{Ni}$ . We also define several quantities used to analyze the wave functions.

### A. Energy variation and generator coordinate method

We use the microscopic  $A$ -body Hamiltonian,

$$\hat{H} = \sum_i^A \hat{t}_i - \hat{t}_{\text{c.m.}} + \frac{1}{2} \sum_{ij}^A \hat{v}_{NN}(ij) + \frac{1}{2} \sum_{ij}^Z \hat{v}_C(ij), \quad (1)$$

where the Gogny D1S interaction [27] is employed as an effective interaction  $\hat{v}_{NN}$  and the Coulomb interaction  $\hat{v}_C$  is approximated by a sum of seven Gaussians. In the AMD framework, the center-of-mass wave function is analytically separable from the internal wave function, and hence, the center-of-mass kinetic energy  $\hat{t}_{\text{c.m.}}$  is exactly removed.

The variational wave function is a parity-projected Slater determinant,

$$\Phi^\pi = \frac{1 + \pi \hat{P}_x}{2} \mathcal{A} \{ \varphi_1, \varphi_2, \dots, \varphi_A \}. \quad (2)$$

Here the single-particle wave packet  $\varphi_i$  is represented by a deformed Gaussian wave packet [28],

$$\varphi_i(\mathbf{r}) = \exp \left[ \sum_{\sigma=x,y,z} -v_\sigma \left( r_\sigma - \frac{Z_{i\sigma}}{\sqrt{v_\sigma}} \right)^2 \right] \chi_i \xi_i, \quad (3)$$

$$\chi_i = \alpha_i \chi_\uparrow + \beta_i \chi_\downarrow, \quad \xi_i = \text{proton or neutron}. \quad (4)$$

The variational parameters are the width  $\mathbf{v}$ , the centroids  $\mathbf{Z}_i$  of Gaussian wave packets, and spin direction  $\alpha_i$  and  $\beta_i$ . They are determined by the variation with the constraints on the matter quadrupole deformation parameters  $\beta$  and  $\gamma$ . The sum of the energy and the constraint potentials,

$$\frac{\langle \Phi^\pi | \hat{H} | \Phi^\pi \rangle}{\langle \Phi^\pi | \Phi^\pi \rangle} + v_\beta (\langle \hat{\beta} \rangle - \beta)^2 + v_\gamma (\langle \hat{\gamma} \rangle - \gamma)^2, \quad (5)$$

is minimized to obtain the optimized wave function  $\Phi^\pi(\beta, \gamma)$  for given values of  $\beta$  and  $\gamma$ . Here  $v_\beta$  and  $v_\gamma$  are sufficiently large values and the definition of  $\langle \hat{\beta} \rangle$  and  $\langle \hat{\gamma} \rangle$  is given in Ref. [26]. In this study, the set of  $(\beta, \gamma)$  is chosen on the triangular lattice in the  $\beta$ - $\gamma$  plane from  $\beta = 0$  to 0.8 at intervals of 0.05.

To complete the calculation, we perform the angular momentum projection and the GCM. The optimized wave function are projected to the eigenstate of  $J^2$ ,

$$\Phi_{MK}^{J\pi}(\beta_i, \gamma_i) = \frac{2J+1}{8\pi^2} \int d\Omega D_{MK}^{J*}(\Omega) \hat{R}(\Omega) \Phi^\pi(\beta_i, \gamma_i), \quad (6)$$

and are superposed employing  $\beta$  and  $\gamma$  as the generator coordinates to describe the eigenstate of  $\hat{H}$ ,

$$\Psi_{M\alpha}^{J\pi} = \sum_{Ki} g_{Ki\alpha}^{J\pi} \Phi_{MK}^{J\pi}(\beta_i, \gamma_i), \quad (7)$$

where the coefficients  $g_{Ki\alpha}^{J\pi}$  and eigenenergies  $E_\alpha^{J\pi}$  are obtained by solving the Hill-Wheeler equation,

$$\sum_{i'K'} H_{KiK'}^{J\pi} g_{K'i'\alpha}^{J\pi} = E_\alpha^{J\pi} \sum_{i'K'} N_{KiK'}^{J\pi} g_{K'i'\alpha}^{J\pi}, \quad (8)$$

$$H_{KiK'}^{J\pi} = \langle \Phi_{MK}^{J\pi}(\beta_i, \gamma_i) | \hat{H} | \Phi_{MK'}^{J\pi}(\beta_{i'}, \gamma_{i'}) \rangle, \quad (9)$$

$$N_{KiK'}^{J\pi} = \langle \Phi_{MK}^{J\pi}(\beta_i, \gamma_i) | \Phi_{MK'}^{J\pi}(\beta_{i'}, \gamma_{i'}) \rangle. \quad (10)$$

### B. Analysis of the wave function

To analyze the structure of the wave function, we define several quantities. We first define the parity-projected and the angular-momentum-projected energies, which are respectively expressed as

$$E^\pi(\beta, \gamma) = \frac{\langle \Phi^\pi(\beta, \gamma) | \hat{H} | \Phi^\pi(\beta, \gamma) \rangle}{\langle \Phi^\pi(\beta, \gamma) | \Phi^\pi(\beta, \gamma) \rangle}, \quad (11)$$

$$E_K^{J\pi}(\beta, \gamma) = \frac{\langle \Phi_{MK}^{J\pi}(\beta, \gamma) | \hat{H} | \Phi_{MK}^{J\pi}(\beta, \gamma) \rangle}{\langle \Phi_{MK}^{J\pi}(\beta, \gamma) | \Phi_{MK}^{J\pi}(\beta, \gamma) \rangle}. \quad (12)$$

For the analysis of the single-particle configuration, we use the principal quantum number of deformed harmonic oscillator

(DHO) defined as

$$N(\beta, \gamma) = \frac{\langle \Phi^\pi(\beta, \gamma) | \hat{N}_{\text{DHO}} | \Phi^\pi(\beta, \gamma) \rangle}{\langle \Phi^\pi(\beta, \gamma) | \Phi^\pi(\beta, \gamma) \rangle}, \quad (13)$$

$$\hat{N}_{\text{DHO}} = \sum_{i=1}^A \sum_{\sigma=x,y,z} \frac{1}{\hbar\omega_\sigma} \left( \frac{p_{i\sigma}^2}{2m} + \frac{m}{2} \omega_\sigma^2 \sigma_i^2 - \frac{1}{2} \right), \quad (14)$$

$$\omega_\sigma = \frac{2\hbar\nu_\sigma}{m} \quad (\sigma = x, y, z). \quad (15)$$

It is noted that the deformation of the DHO potential is defined depending on the deformation of the Gaussian wave packets of  $\Phi^\pi(\beta, \gamma)$ . Therefore,  $N(\beta, \gamma)$  roughly estimates the configuration in the DHO potential. In the case of  $^{56}\text{Ni}$ , the lowest Pauli allowed value of  $N$  is  $N_{\text{min}} = 108$ .

The direct information of the single-particle configuration is obtained by the single-particle energy and wave function which are calculated as follows. We first transform the single-particle wave packets  $\varphi_i$  of  $\Phi^\pi(\beta, \gamma)$  into the orthonormalized basis  $\tilde{\varphi}_p$ ,

$$\tilde{\varphi}_p = \frac{1}{\sqrt{\mu_p}} \sum_i c_{ip} \varphi_i, \quad (16)$$

where  $\mu_p$  and  $c_{ip}$  are the eigenvalues and the eigenvectors of the overlap matrix  $B_{ij} = \langle \varphi_i | \varphi_j \rangle$ . Note that this transformation does not change the Slater determinant except for a trivial factor. Then we construct the single-particle Hamiltonian,

$$h_{pq} = \langle \tilde{\varphi}_p | \hat{h} | \tilde{\varphi}_q \rangle + \sum_r \langle \tilde{\varphi}_p \tilde{\varphi}_r | \hat{v} | \tilde{\varphi}_q \tilde{\varphi}_r \rangle - \tilde{\varphi}_r \tilde{\varphi}_q. \quad (17)$$

The eigenvalues and eigenvectors of  $h_{pq}$  give the single-particle energies and wave functions,

$$\sum_q h_{pq} f_{q\alpha} = \epsilon_\alpha f_{p\alpha}, \quad (18)$$

$$\phi_\alpha = \sum_p f_{p\alpha} \tilde{\varphi}_p = \sum_i \left( \sum_p c_{ip} \frac{1}{\sqrt{\mu_p}} f_{p\alpha} \right) \varphi_i. \quad (19)$$

Finally, we define the GCM amplitude  $O_{K\alpha}^{J\pi}$ , which is the overlap between  $\Psi_{M\alpha}^{J\pi}$  and the basis wave function  $\Phi_{MK}^{J\pi}$  to

discuss the distribution of the wave function in the  $\beta$ - $\gamma$  plane,

$$O_{K\alpha}^{J\pi}(\beta, \gamma) = \left| \langle \Phi_{MK}^{J\pi}(\beta, \gamma) | \Psi_{M\alpha}^{J\pi} \rangle \right|^2. \quad (20)$$

This amplitude reflects the properties of each states such as the SD band,  $\beta$  vibration, and so on.

### III. RESULTS AND DISCUSSIONS

#### A. Energy surfaces and single-particle configurations

Figure 1(a) shows the parity-projected energy surface of the positive-parity states obtained by the variational calculation. It can be classified into two regions depending on the expectation values of the principal quantum number  $N(\beta, \gamma)$  shown in Fig. 1(b). In the region with  $\beta \leq 0.5$ ,  $N(\beta, \gamma)$  is approximately equal to  $N_{\text{min}}$ , and hence, these wave functions are dominated by  $0\hbar\omega$  configurations in the deformed mean field; i.e., all valence nucleons are within the orbits originate in the spherical  $pf$  shell. In this region, there are the global energy minimum at  $(\beta, \gamma) = (0.0, 0^\circ)$  and a local minimum at  $(0.35, 0^\circ)$ . The energy surface with  $0\hbar\omega$  configurations is quite flat against  $\gamma$  deformation and soft against  $\beta$  deformation. For example, the energy differences between the states at  $(\beta, \gamma) = (0.0, 0^\circ), (0.35, 0^\circ)$ , and  $(0.30, 60^\circ)$  are within 8 MeV.

The single-particle configuration and the  $N = Z = 28$  shell gap change depending on  $\beta$  and  $\gamma$  as shown in Fig. 2, in which neutron single-particle energies are plotted along a path shown in Fig. 1(a). In the present result, protons and neutrons are always excited simultaneously; therefore, only the neutron single-particle energies are shown. The change of single-particle energies shows the existence of various configurations in the  $\beta \leq 0.5$  region. In the spherical shape, the lowest configuration is the  $f_{7/2}$  closed-shell configuration. The  $N = Z = 28$  shell gap at spherical shape decreases as the prolate deformation grows and the intruder orbit originating in the spherical  $p_{3/2}$  orbit ( $[310, 1/2]$  orbit in Nilsson model) becomes lower than one of the orbit originates in spherical the  $f_{7/2}$  orbit around  $\beta = 0.25$ . In the prolate deformed region with  $0.25 \leq \beta \leq 0.4$ , where the spherical shell gap is lost but a deformed  $N = Z = 28$  shell gap exists, a deformed  $(f_{7/2})^{-4}(p_{3/2})^4$  configuration appears. In the

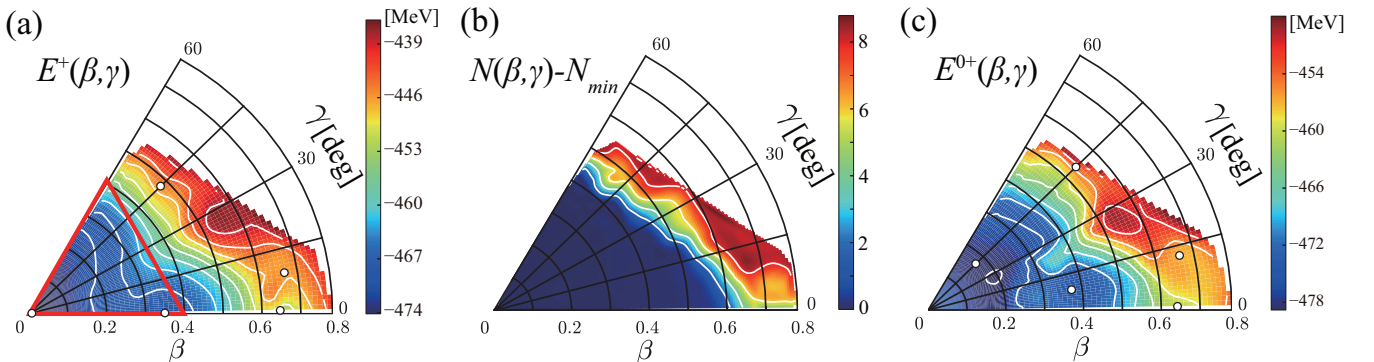


FIG. 1. (Color online) (a) The parity-projected energy surface before the angular momentum projection. The red line shows the path along which the neutron single-particle energies are plotted in Fig. 2. (b) The principal quantum number of DHO calculated from the parity-projected wave function shown in (a). (c) The angular-momentum-projected energy surface of the  $J^\pi = 0^+$  states. The open circles in (a) and (c) show the positions of the global and local energy minima.

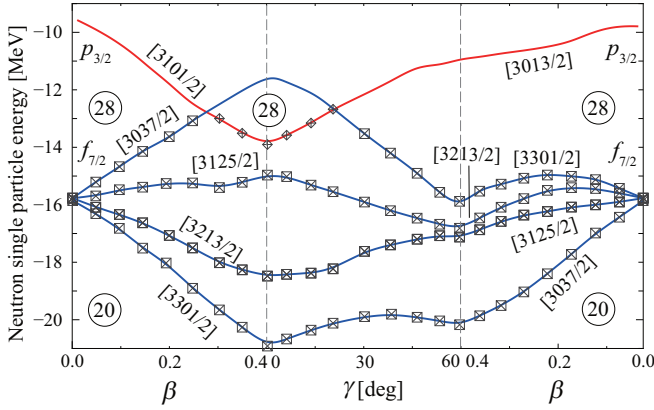


FIG. 2. (Color online) The neutron single-particle energies along the path shown in Fig. 1(a). The lines with symbols show the orbits occupied in the lowest energy configuration, while those without symbols show the unoccupied orbits.

triaxially deformed region, the order of the orbits originating in the spherical  $f_{7/2}$  and  $p_{3/2}$  orbits is reverted around  $\gamma = 20^\circ$ . In the oblate side, the intruder orbit from  $p_{3/2}$  stays much higher than  $f_{7/2}$  and the spherical  $N = Z = 28$  shell gap is kept large. Therefore, the oblately deformed states are dominated by the configuration originates in the spherical  $f_{7/2}$  closed configuration.

In  $\beta \geq 0.5$  region, an intruder orbit from  $g_{9/2}$  becomes lower than the orbits that originate in  $f_{7/2}$  and  $p_{3/2}$ , and hence, the configurations with  $g_{9/2}$  appear and make the  $N(\beta, \gamma)$  larger than  $N_{\min}$ . A strongly prolate deformed local energy minimum appears at  $(\beta, \gamma) = (0.64, 0^\circ)$ , which has a  $(f_{7/2})^{-8}(p_{3/2})^4(g_{9/2})^4$  configuration. The increase of  $\gamma$  from the prolate side toward the oblate side brings about the crossings of an orbit that originates in  $d_{3/2}$  with  $f_{7/2}$  and  $p_{3/2}$ . These level crossings generate two strongly deformed minima with axial asymmetric shapes at  $(\beta, \gamma) = (0.66, 8^\circ)$  and  $(0.54, 55^\circ)$  which have the configurations of  $(d_{3/2})^{-4}(f_{7/2})^{-4}(p_{3/2})^4(g_{9/2})^4$  and  $(d_{3/2})^{-4}(g_{9/2})^4$ , respectively.

By the angular momentum projection, the deformed states gain larger energy than the spherical states, and energy surface becomes more soft against  $\beta$  and  $\gamma$  deformations. As a result, the energy minima on the surface move toward larger deformations. Figure 2(c) shows the energy surface after the angular momentum projection to  $J^\pi = 0^+$ . In the  $\beta \leq 0.5$  region, the global and local minima move to  $(\beta, \gamma) = (0.18, 45^\circ)$  and  $(0.38, 8^\circ)$  after the angular momentum projection. They gain 2.5- and 5.2-MeV binding energies by the projection, respectively. Note that the global minimum is not a spherical state despite of the  $N = Z = 28$  shell closure and both minima are not axially symmetric as seen in their intrinsic density distributions in Figs. 3(a) and 3(b). In the  $\beta \geq 0.5$  region, strongly deformed minima with  $g_{9/2}$  configurations also move to  $(\beta, \gamma) = (0.64, 0^\circ)$ ,  $(0.66, 14^\circ)$ , and  $(0.53, 45^\circ)$ , and their energy gains by the projection are 13.8, 11.8, and 12.9 MeV, respectively. The density distributions of the prolate and axially asymmetric deformed minima [Figs. 3(c)–3(e)] show

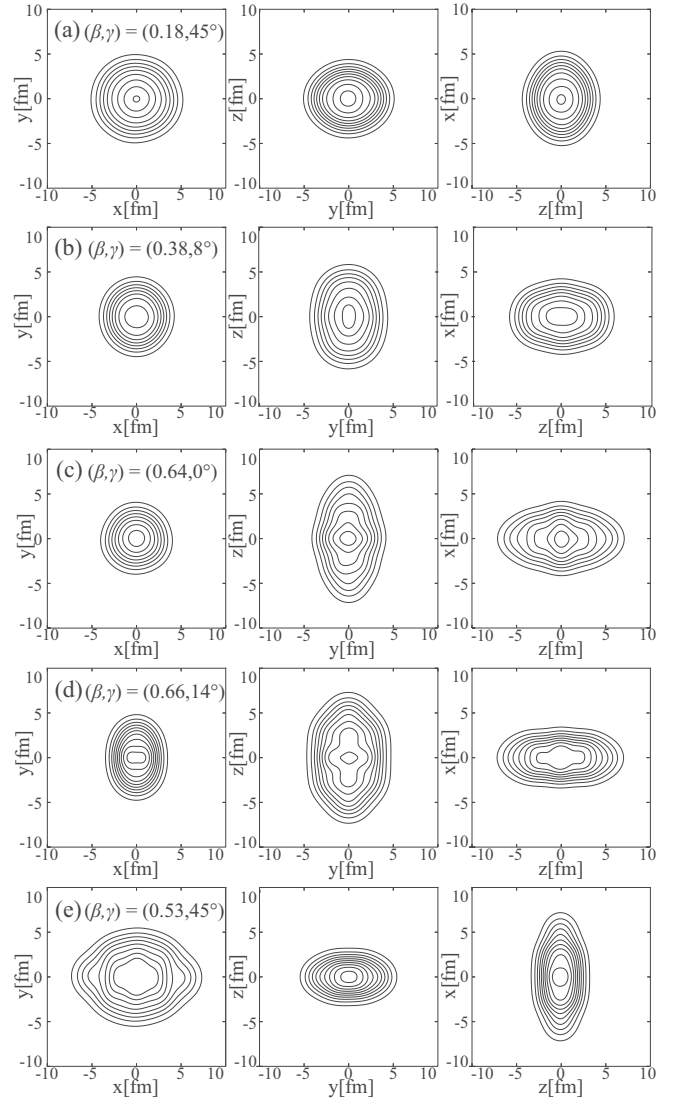


FIG. 3. Intrinsic density distribution of (a) the global minimum at  $(\beta, \gamma) = (0.18, 45^\circ)$ , (b) the prolate minimum at  $(\beta, \gamma) = (0.38, 8^\circ)$ , and the strongly deformed local energy minima with  $g_{9/2}$  configurations located at (c)  $(\beta, \gamma) = (0.64, 0^\circ)$ , (d)  $(\beta, \gamma) = (0.66, 14^\circ)$ , and (e)  $(\beta, \gamma) = (0.53, 45^\circ)$ .

that the ratios of the deformation axis are approximately equal to 1:2.

To summarize this section, we remind the reader of the following three points. (1) Despite the double magic number of  $N = Z = 28$ ,  $^{56}\text{Ni}$  is unstable against the oblate deformation. The global energy minimum is slightly deformed and located at  $(\beta, \gamma) = (0.18, 45^\circ)$ . (2) In the prolate deformed region, the SD shell gap replaces the spherical one owing to the inversion of orbits originate in the spherical  $f_{7/2}$  and  $p_{3/2}$  orbits, and there exists a local minimum with a  $(f_{7/2})^{-4}(p_{3/2})^4$  configuration at  $(\beta, \gamma) = (0.38, 8^\circ)$ . (3) In the strongly deformed region ( $\beta \geq 0.5$ ), the configurations involving the  $g_{9/2}$  orbit appear. There are three minima with  $(f_{7/2})^{-8}(p_{3/2})^4(g_{9/2})^4$ ,  $(d_{3/2})^{-4}(f_{7/2})^{-4}(p_{3/2})^4(g_{9/2})^4$ , and  $(d_{3/2})^{-4}(g_{9/2})^4$  configurations, of which deformations are close to a 1:2 ratio.

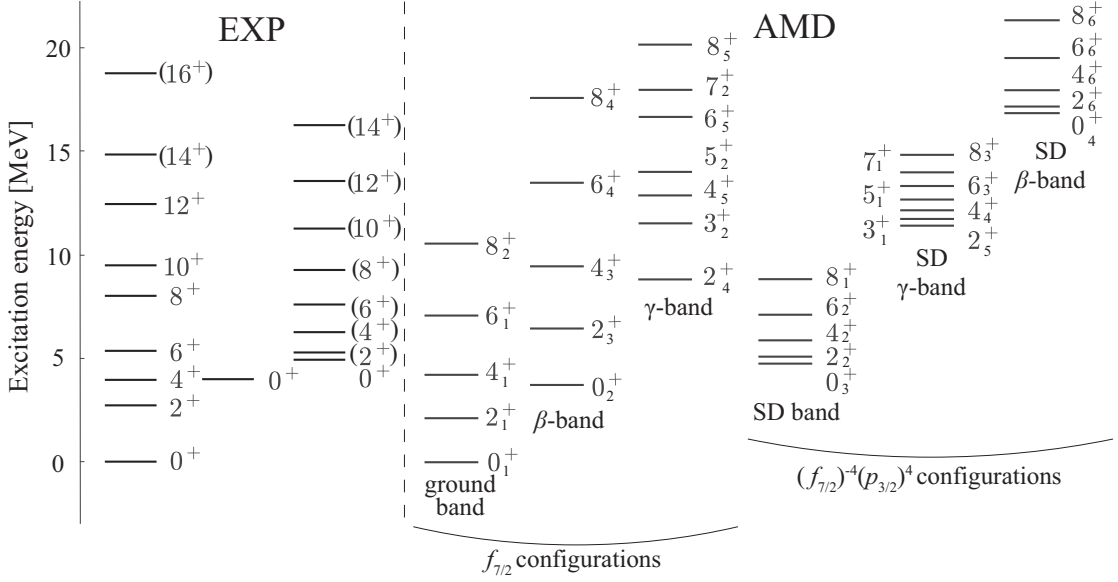


FIG. 4. Low-lying positive-parity states up to  $J^\pi = 8^+$  obtained by the GCM calculation. The observed spectrum [1,12] is also shown for the sake of the comparison.

### B. Low-lying states with $pf$ -shell configurations

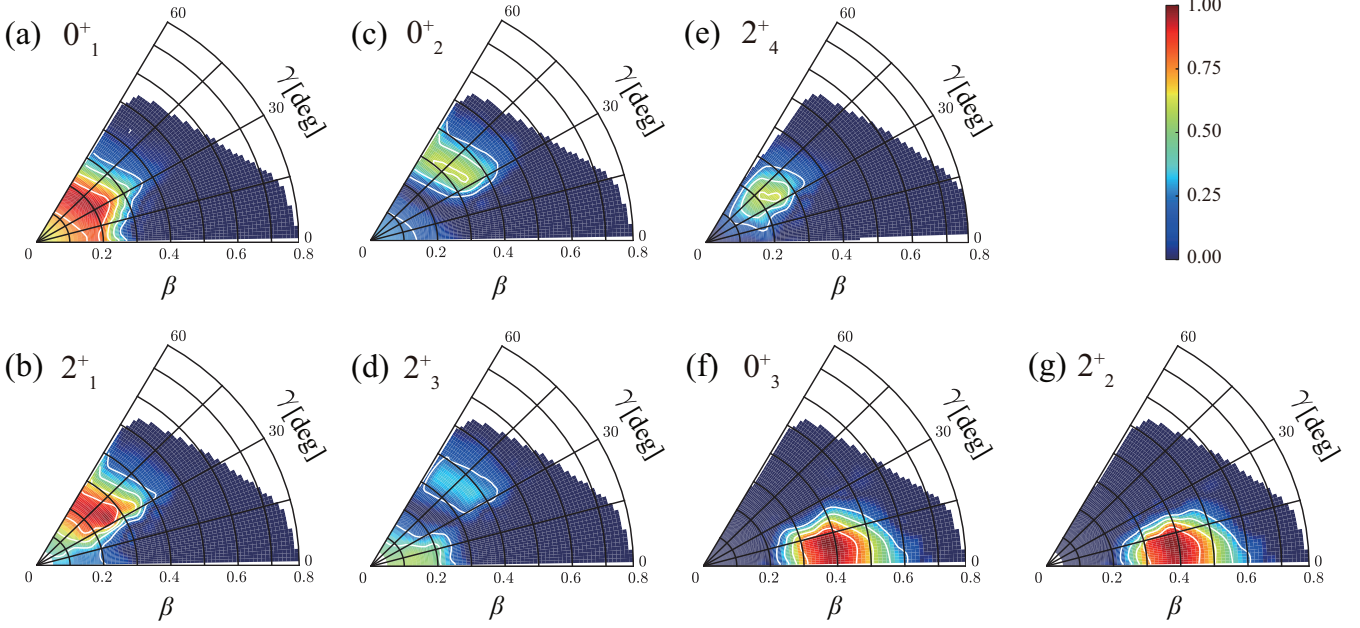
In this section, we focus on the low-lying states dominated by the  $(f_{7/2})^{-m}(p_{3/2})^m$  configurations. Figure 4 shows the low-lying six bands obtained by the GCM calculation up to  $J^\pi = 8^+$  states, and the band assignment is based on the strong in-band  $E2$  transitions listed in Table I. There is an almost spherical band built on the ground state and two oblate deformed bands starting from the  $0_2^+$  state at  $E = 3.7$  MeV and from the  $2_4^+$  state at 8.9 MeV, which are denoted as the ground,  $\beta$  and  $\gamma$  bands, respectively. These three bands are composed of the spherical and oblate deformed intrinsic states with  $f_{7/2}$  configurations. The intrinsic states in the vicinity of a prolate deformed minimum with an  $(f_{7/2})^{-4}(p_{3/2})^4$  configuration generate three well-deformed rotational bands in Fig. 4. They are the SD band with  $K^\pi = 0^+$  built on the  $0_3^+$  state at 4.7 MeV, the SD  $\gamma$  band with  $K^\pi = 2^+$  on the  $2_5^+$  at 11.3 MeV, and the SD  $\beta$  band with  $K^\pi = 0^+$  on the  $0_4^+$  state at 17.0 MeV.

The calculated ground-band spectrum does not reproduce observed irregular level spacing, especially those of  $0^+-2^+$  and  $6^+-8^+$ . The MCSM calculation [6] which successfully reproduced the observed level spacing suggested that the occupation number of the  $f_{7/2}$  orbital varies depending on the angular momentum. Therefore, the irregular level spacing may be closely related to the occupation number of  $f_{7/2}$  orbital in each yrast state. This feature may be included by performing the angular momentum projection before the variation which optimizes the intrinsic wave function for each angular momentum state. However, it costs too much computational time and did not perform in the present study. The properties of the band member states are identified from their GCM amplitudes shown in Figs. 5(a) and 5(b). The amplitude of the ground state distributes in a small deformed region, and its maximum is at  $(\beta, \gamma) = (0.18, 45^\circ)$ , indicating weak oblate deformation in spite of the double magic number  $N = Z = 28$ . From the GCM amplitude, it is also found that

the closed-shell configuration amounts to only 62% in the ground state, which agrees with the MCSM results [5–10].

TABLE I. The in-band  $E2$  transition probability  $B(E2)$  and the monopole matrix element  $M(E0)$  between the ground and  $\beta$  bands. In the first column,  $g$ ,  $\beta$ , SD, and SD  $\beta$  represent the ground,  $\beta$ , SD, and SD  $\beta$ -bands, respectively.

Band	$J_i^\pi$	$J_f^\pi$	$B(E2)$ ( $e^2 \text{fm}^4$ )
$g \rightarrow g$	$2_1^+$	$0_1^+$	182(112) [2–4]
	$4_1^+$	$2_1^+$	306
	$6_1^+$	$4_1^+$	338
	$8_2^+$	$6_1^+$	508
$\beta \rightarrow \beta$	$2_3^+$	$0_2^+$	187
	$4_3^+$	$2_3^+$	155
	$6_4^+$	$4_3^+$	246
	$8_4^+$	$6_4^+$	382
SD $\rightarrow$ SD	$2_2^+$	$0_3^+$	808
	$4_2^+$	$2_2^+$	1143
	$6_2^+$	$4_2^+$	1236
	$8_1^+$	$6_2^+$	1268
			$M(E0)$ ( $\text{fm}^2$ )
$g \rightarrow \beta$	$0_1^+$	$0_2^+$	7.85
	$2_1^+$	$2_3^+$	8.44
	$4_1^+$	$4_3^+$	5.96
	$6_1^+$	$6_4^+$	8.14
	$8_2^+$	$8_4^+$	8.49
SD $\rightarrow$ SD $\beta$	$0_3^+$	$0_4^+$	11.8
	$2_2^+$	$2_6^+$	11.7
	$4_2^+$	$4_6^+$	11.4
	$6_2^+$	$6_6^+$	10.4
	$8_1^+$	$8_6^+$	10.1

FIG. 5. (Color online) The GCM amplitudes of the low-lying  $0^+$  and  $2^+$  states.

In a simple shell-model description, the  $2_1^+$  state is a spherical state with an  $(f_{7/2})^{-1}(p_{3/2})^1$  configuration and located at rather high excitation energy corresponding to the  $N = Z = 28$  shell gap. However, the observed  $2_1^+$  state is at 2.7 MeV and the calculated  $2_1^+$  state also locates at small energy,  $E = 2.1$  MeV. The amplitude of the  $2_1^+$  state shows a different nature from a simple picture; i.e., it is oblately deformed and oriented at  $(\beta, \gamma) = (0.23, 49^\circ)$ . This indicates the softness or instability of the  $f_{7/2}$  closed configuration against oblate deformation. The origin of this softness can be seen in Fig. 2, which shows that the spherical  $f_{7/2}$  closed configuration can be easily deformed toward the oblate side without changing the configuration and without reducing the  $N = Z = 28$  shell gap. The oblate deformation leads to the relatively large  $B(E2; 2_1^+ \rightarrow 0_1^+) = 182 e^2 \text{ fm}^4$ , which is comparable with the observed value of  $112 e^2 \text{ fm}^4$  (8.8 W.u.) [2–4]. Other member states such as the  $4_1^+$  state show similar amplitudes to the  $2_1^+$  state, and hence, the in-band  $B(E2)$  are large. However, the overestimation of  $B(E2; 2_1^+ \rightarrow 0_1^+)$  implies that the actual deformation of  $^{56}\text{Ni}$  is smaller than the present result.

The existence of the  $\beta$  band built on the  $0_2^+$  state at 3.7 MeV also indicates the softness against oblate deformation. The calculated  $0_2^+$  state is located at 3.7 MeV, which fairly agrees with the observation, although other member states have not been observed yet. The GCM amplitudes of the  $0_2^+$  and  $2_3^+$  states [Figs. 5(c) and 5(d)] show the  $\beta$ -vibrational character of this band. Namely, their amplitudes are widely distributed toward the oblate side and have a node around  $\beta = 0.2$  to be orthogonal to the member states of the ground band. Therefore, we conclude that this band is a  $\beta$  band built on the ground band by the oscillation in the direction of the oblate deformation. The interpretation of the  $\beta$  band is supported by the large monopole matrix element  $M(E0)$  between the ground and  $\beta$  bands, which is well known to be enhanced as large as the single-particle unit. Assuming a uniform density distribution,

the single-particle unit is estimated as  $M_{\text{sp}}(E0) = 11 \text{ fm}^2$  for  $^{56}\text{Ni}$ , while the matrix element between the ground and  $\beta$  bands can be expressed as [29]

$$M_\beta(E0) = 2\beta_0 \left( \frac{3}{4\pi} ZR^2 \right) \left[ 1 + \frac{4}{3} \pi^2 \left( \frac{a}{R} \right)^2 \right] \Delta\beta, \quad (21)$$

where  $\beta_0$  is the equilibrium value of  $\beta$ ,  $\Delta\beta$  is the amplitude of the oscillation, and  $a$  is the diffuseness of the nuclear density. For example, putting  $\beta_0 = 0.18$ ,  $\Delta\beta = 0.1$ , and  $a = 0.54 \text{ fm}$  by referring the present result, it is estimated as  $M_\beta(E0) = 6 \text{ fm}^2$ , which is comparable with  $M_{\text{sp}}(E0)$ . As listed in Table I, the calculated  $M(E0)$  are also as large as  $M_{\text{sp}}(E0)$  and  $M_\beta(E0)$ .

We also comment on the deviation of spectrum of the  $\beta$  band from the rotation-vibration model. For example, Figs. 5(a)–5(d) show that the equilibrium of  $\beta$  vibration is different for  $0^+$  and  $2^+$  states. The  $2_1^+$  and  $2_3^+$  states have slightly larger equilibrium value of  $\beta = 0.23$  that leads to the different distribution of GCM amplitudes between the  $0_1^+$  and  $2_1^+$  states and between the  $0_2^+$  and  $2_3^+$  states. In particular, the  $0_2^+$  state has large amplitude around  $\beta = 0.3$ , which overlaps well with that of the  $2_1^+$  state. As a result,  $B(E2; 2_1^+ \rightarrow 0_2^+)$  has large value of  $112 e^2 \text{ fm}^4$  comparable with  $B(E2; 2_1^+ \rightarrow 0_1^+)$ .

In contrast to the  $\beta$  band, the relatively high excitation energy of the  $\gamma$  band shows that the  $f_{7/2}$  configurations are not as soft against the  $\gamma$  deformation as they are in the  $\beta$  deformation. This band is built on the  $2_4^+$  state at 8.9 MeV, which is much higher than the  $\beta$  band. Because the member states of this band are dominantly composed of the wave function with  $K^\pi = 2^+$  and the GCM amplitudes have similar distributions to the ground band with slight shift toward the  $\gamma$  deformation, we interpret this band as the  $\gamma$  band built on the ground band.

The SD band is built on the  $0_3^+$  state at 4.7 MeV and has large moment of inertia,  $\hbar^2/2I = 56$  keV. Almost the same results are also obtained by MCSM calculations [6,7] and both of the present and the MCSM results fairly agree with the observed bandhead energy  $E = 5.0$  MeV and the moment of inertia  $\hbar^2/2I = 61$  keV, reported by Rudolph *et al.* [11]. Owing to large deformation, the in-band  $B(E2)$  are much larger than those in the ground,  $\beta$ , and  $\gamma$  bands. The GCM amplitudes [Figs. 5(f) and 5(g)] are concentrated around the prolate side  $(\beta, \gamma) = (0.38, 8^\circ)$ , where the inversion of orbits that originate in the spherical  $f_{7/2}$  and  $p_{1/2}$  orbits ([303, 7/2] and [310, 1/2]) takes place. Therefore, the SD band has a  $(f_{7/2})^{-4}(p_{3/2})^4$  configuration and the  $B(E2)$  between the other bands with the  $f_{7/2}$  configurations is very small and less than  $1.0 e^2 \text{ fm}^4$ . It is notable that the excitation energy of the  $0_3^+$  state is rather small in spite of the four-particle excitation. This suggests that the  $N = Z = 28$  shell gap easily disappears and the deformed shell gap appears by the prolate deformation.

Similar to the ground band, the SD band is also accompanied by the SD  $\beta$  band built on the  $0_4^+$  state at 16.9 MeV and the SD  $\gamma$  band built on the  $2_5^+$  state at 11.3 MeV. The GCM amplitude of the SD  $\beta$  band is oriented around  $(\beta, \gamma) = (0.53, 12^\circ)$  and that of the SD  $\gamma$  band is around  $(0.40, 18^\circ)$ . However, different from the ground band, the energy of the SD  $\beta$  and  $\gamma$  bands are rather high, because the energy surface around the SD minimum  $[(\beta, \gamma) = (0.38, 8^\circ)]$  is much steeper than that around the ground state. It is also noted that  $M(E0)$  between the SD and SD  $\beta$  bands is also large (Table I) and are comparable with  $M_{\text{sp}}(E0)$  and  $M_{\beta}(E0) = 11 \text{ fm}^2$  estimated by Eq. (21) setting  $\beta_0 = 0.38$  and  $\Delta\beta = 0.1$ .

To close this section, we summarize the discussion in this section. Owing to the instability against oblate deformation, the ground state is oblately deformed and the  $N = Z = 28$  closed-shell configuration amounts to only 62%. We predict the existence of the  $\beta$  band as a signature of the instability against oblate deformation. It is also found that the prolate deformed shell gap generates the SD band with a  $(f_{7/2})^{-4}(p_{3/2})^4$  configuration. The present calculation reproduces the excitation energies of the  $0_2^+$  state and SD band; however, it fails to reproduce the ground band spectrum and  $B(E2; 2_1^+ \rightarrow 0_1^+)$ . To improve the description of the ground band, it is needed to perform the variation after the angular momentum projection and to try other effective interactions. It should be noted that, by these improvements, the present result might be changed quantitatively.

### C. Highly excited and strongly deformed bands with $g_{9/2}$ configurations

In the highly excited region above  $E = 20$  MeV, we have obtained four strongly deformed rotational bands shown in Fig. 6. As discussed below in detail, the maxima of their GCM amplitudes correspond to the minima on the energy surface with  $\beta \geq 0.5$ , and, hence, they have the configurations involving the orbit originates in the spherical  $g_{9/2}$ . Depending on the single-particle configurations, we classified them into three groups, which we call bands 1, 2, and 3. Their properties such as the moment of inertia and in-band  $B(E2)$  strengths are listed in Tables II and III, respectively. Because their excitation

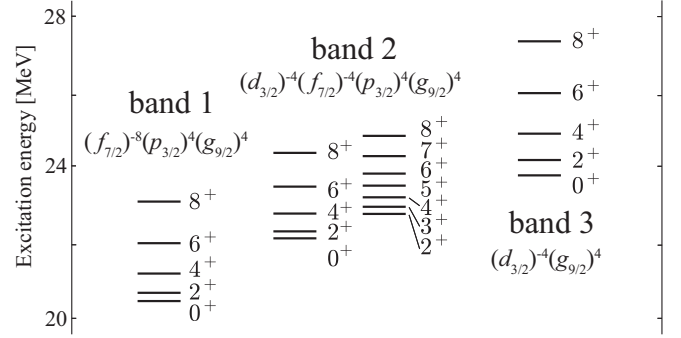


FIG. 6. Four rotational bands with the configurations involving the  $g_{9/2}$  orbit located above  $E_x = 20$  MeV. Depending on their configurations, they are classified to three groups, bands 1, 2, and 3.

energies and the moments of inertia are very large, they possibly associated with the resonant structure observed in  $^{28}\text{Si}(^{28}\text{Si}, ^{28}\text{Si}^*)^{28}\text{Si}^*$  reactions [14,15]. Therefore, we discuss their properties by comparing the observed data and other theoretical calculations such as the  $\alpha$  cluster model [18], Nilsson model [19], and Skyrme Hartree-Fock model [22].

Band 1 starting from  $E = 20.8$  MeV has the maximum of GCM amplitude at  $(\beta, \gamma) = (0.74, 0^\circ)$  and has a configuration of  $(f_{7/2})^{-8}(p_{3/2})^4(g_{9/2})^4$ . This band has prolate shape with axial symmetry, as seen in its intrinsic density distribution and the ratio of the shortest, the middle, and the longest axes is 1.0:1.0:1.9. A similar prolate band was also reported in the  $\alpha$ -cluster model (denoted as 2:1 band) [18] and the Nilsson model [19] studied. They suggested the same single-particle configuration with the present result and the Nilsson model study showed that the axis ratio is 1:1:1.8, which is very close to the present result. The rotational energies of the prolate deformed band are plotted in Fig. 7. The red solid and dashed lines correspond to band 1 and the 2:1 band in the  $\alpha$ -cluster model, respectively. Their moments of inertia are very close to each other and they are considered to be an identical band. It is also noted that the  $\alpha$ -cluster model study showed that the single-particle configuration of 2:1 band corresponds to the  $^{40}\text{Ca} + ^{16}\text{O}$ -cluster configuration by applying Harvey prescription [30].

Band 2 consists of  $K^\pi = 0^+$  and  $2^+$  bands starting from  $E = 21.8$  and 22.8 MeV, respectively. They have an

TABLE II. The deformation parameters, the ratio of the deformed axis, and the moment of inertia of the strongly deformed  $K^\pi = 0^+$  bands. The intrinsic axis is taken to be  $\langle x^2 \rangle \leq \langle y^2 \rangle \leq \langle z^2 \rangle$ .

	Band 1	Band 2	Band 3
$\beta$	0.74	0.66	0.53
$\gamma$	$0^\circ$	$14^\circ$	$45^\circ$
$\sqrt{\langle x^2 \rangle}$ (fm)	1.76	1.54	1.42
$\sqrt{\langle y^2 \rangle}$	1.76	2.09	2.57
$\sqrt{\langle z^2 \rangle}$	3.35	3.21	2.86
$\sqrt{\langle x^2 \rangle} : \sqrt{\langle y^2 \rangle} : \sqrt{\langle z^2 \rangle}$	1.0:1.0:1.9	1.0:1.3:2.1	1.0:1.8:2.0
$\hbar^2/2I$ (keV)	36	32	50

TABLE III. The reduced transition probability  $B(E2)$  values in the highly excited states.

Band	$J_i$	$J_f$	$B(E2)$ ( $e^2 \text{fm}^4$ )
1	$2^+$	$0^+$	3944
	$4^+$	$2^+$	5641
	$6^+$	$4^+$	6227
	$8^+$	$6^+$	6538
2	$2^+$	$0^+$	3203
	$4^+$	$2^+$	1922
	$6^+$	$4^+$	2235
	$8^+$	$6^+$	4527
3	$2^+$	$0^+$	1909
	$4^+$	$2^+$	2887
	$6^+$	$4^+$	3242
	$8^+$	$6^+$	3473

$(f_{7/2})^{-4}(d_{3/2})^{-4}(p_{3/2})^4(g_{9/2})^4$  configuration and the maximum of their GCM amplitudes are located at  $(\beta, \gamma) = (0.66, 14^\circ)$ . The ratio of deformation axis is 1.0:1.3:2.1. Triaxially deformed states are also reported by the  $\alpha$ -cluster model (denoted as triaxial band) and the Nilsson model calculations. The triaxial state in the  $\alpha$ -cluster model has the similar moment of inertia and the Nilsson model predicted the similar ratio of axis (1.0:1.2:2.1) to present result. However, these triaxially deformed states are different from each other, because their configurations are different to each other; that is, they have  $8\hbar\omega$ ,  $16\hbar\omega$ , and  $12\hbar\omega$  configurations in the present, the  $\alpha$ -cluster model and the Nilsson model calculations, respectively.

Band 3 starting from  $E = 23.8$  MeV has the maximum of the GCM amplitude at  $(\beta, \gamma) = (0.53, 45^\circ)$  and has a configuration of  $(d_{3/2})^{-4}(g_{9/2})^4$ . The ratio of deformation axis is 1.0:1.8:2.0. In the Skyrme Hartree-Fock model calculation [22], a similar state was reported as a local minimum

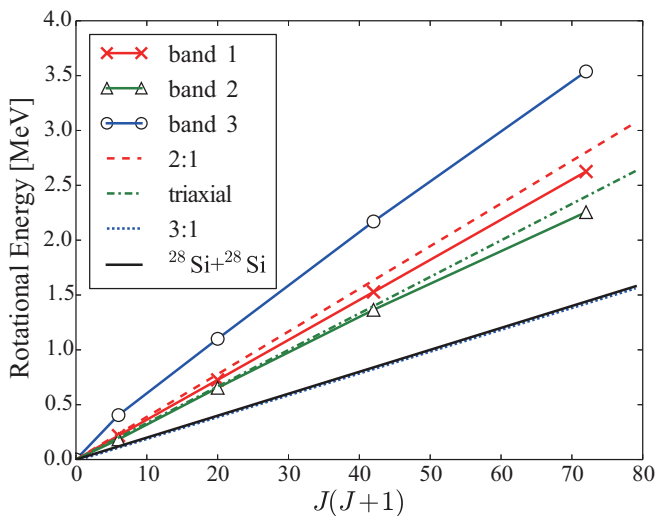


FIG. 7. (Color online) The rotational energies for highly excited states above  $E = 20$  MeV and 2:1, triaxial, and 3:1 bands reported in the  $\alpha$ -cluster model calculation [18] and the observed  $^{28}\text{Si}(^{28}\text{Si}, ^{28}\text{Si}^*)^{28}\text{Si}^*$  resonance states [14]. The observed data are extrapolated to lower  $J$  by  $E_{\text{rot}} = \hbar^2 J(J+1)/2I$ .

in the energy curve located at  $(\beta, \gamma) = (0.598, 60^\circ)$  and  $E = 21.5$  MeV. The moment of inertia of band 3 is rather smaller than those of bands 1 and 2.

To end this section, we comment on the relationship between the present results and the observed  $^{28}\text{Si}(^{28}\text{Si}, ^{28}\text{Si}^*)^{28}\text{Si}^*$  resonances. In Fig. 7, the rotational energies in which the observed data are extrapolated to the lower  $J$  are plotted with the black solid line. In present result, there are no bands that have the moment of inertia corresponding to the observed resonance, even though we have predicted several bands with large deformations. It is also noted that only the “3:1 band” reported by the  $\alpha$ -cluster model explains the observed large moment of inertia. This fact may mean that it is necessary to include the degree of freedom of clustering explicitly into the present theoretical framework to explain the observed resonances. The results of such calculation will be reported in our next work.

#### IV. SUMMARY

In this paper, we have studied the coexistence of various structures in the low-lying states of  $^{56}\text{Ni}$  and how the spherical  $N = Z = 28$  shell gap is weakened. We also explored the highly excited and strongly deformed state and examined their relationship with the results of the other theoretical models and the observed data.

The energy surface and single-particle energies as functions of the quadrupole deformation obtained by the variational calculation with AMD showed that the  $f_{7/2}$  closed configuration is unstable against the oblate deformation. As a result, it is found that the ground band is slightly deformed and the  $N = Z = 28$  closed-shell configuration amounts to only 62% in the ground state. The calculated  $E(2_1^+) = 2.1$  MeV and the  $B(E2; 2_1^+ \rightarrow 0_1^+) = 182 e^2 \text{fm}^4$  indicate the enhanced collectivity owing to the deformation. Furthermore, as a signature of the instability against oblate deformation, we predicted the existence of the low-lying  $K = 0^+$  band built on the  $0_2^+$  state which has a  $\beta$ -vibrational nature. The  $\beta$ -vibrational nature of this band is confirmed by the enhancement of the  $E0$  matrix element  $M(E0)$  comparable with the single-particle unit. We also predict the  $K^\pi = 2^+$  band built on the  $2_4^+$  state at 8.9 MeV. However, the present calculation fails to reproduce the ground-band spectrum and  $B(E2; 2_1^+ \rightarrow 0_1^+)$ . The description of the ground band may be improved by performing the variation after the angular momentum projection and trying other effective interactions. Therefore, it is noted that the present result might be changed quantitatively by the improvement.

In contrast to oblate deformation, prolate deformation brings about the inversion between the orbitals that originate in  $p_{3/2}$  and  $f_{7/2}$ , and it generates the deformed  $N = Z = 28$  shell gap around  $\beta = 0.4$  instead of the spherical shell gap. As a result, the SD band with an  $(f_{7/2})^{-4}(p_{3/2})^4$  configuration appears at  $E = 4.7$  MeV, which plausibly reproduces the observed data. We also predict the  $\beta$ - and  $\gamma$ -vibrational bands that accompany the SD band, which are respectively located at  $E = 11.3$  and 17.0 MeV.

In the  $\beta \geq 0.5$  region of prolate deformation, an intruder orbit from  $g_{9/2}$  becomes lower than the orbits that originate in

$f_{7/2}$  and  $p_{3/2}$ , and the increase of  $\gamma$  from the prolate side to the oblate side brings about the crossings of an orbit that originates in  $d_{3/2}$  with  $f_{7/2}$  and  $p_{3/2}$ . As a result, three strongly deformed minima are generated. Corresponding to these minima, four strongly deformed bands which are classified into three groups of bands 1, 2, and 3 are obtained above  $E = 20$  MeV. Band 1 has prolate shape and has an  $(f_{7/2})^{-8}(p_{3/2})^4(g_{9/2})^4$  configuration. The similar states are reported in the  $\alpha$ -cluster model and the Nilsson model calculations. Band 2 is triaxially deformed with a 1.0:1.3:2.1 ratio of the deformation axis. Its configuration is identified as  $(f_{7/2})^{-4}(d_{3/2})^{-4}(p_{3/2})^4(g_{9/2})^4$ . Owing to triaxially deformation, the  $K^\pi = 2^+$  side band appears. The triaxially deformed states are also obtained in the  $\alpha$ -cluster model and the Nilsson model but their configurations

are different from each other. Band 3 has an oblate shape and has a ratio of axis 1.0:1.8:2.0. The configuration of this band is  $(d_{3/2})^{-4}(g_{9/2})^4$ . These four bands have smaller moments of inertia than those of the resonance states observed in Refs. [14,15].

#### ACKNOWLEDGMENTS

The numerical calculations were performed on the HITACHI SR16000 at KEK and YITP. One of the authors (M.K.) acknowledges that this work is supported by the Grants-in-Aid for Scientific Research on Innovative Areas from MEXT (Grant No. 2404:24105008) and JSPS KAKENHI Grant No. 25400240.

- 
- [1] J. Huo, S. Huo, and D. Young, *Nucl. Data Sheets* **112**, 1513 (2011).
- [2] G. Kraus *et al.*, *Phys. Rev. Lett.* **73**, 1773 (1994).
- [3] Y. Yanagisawa *et al.*, in *Proceedings ENAM 98, Exotic Nuclei and Atomic Masses*, edited by B. M. Sherrill, D. J. Morrissey, and C. N. Davids, AIP Conference Proceedings 455 (AIP, Woodbury, NY, 1998), p. 610.
- [4] K. L. Yurkewicz *et al.*, *Phys. Rev. C* **70**, 054319 (2004).
- [5] T. Otsuka, M. Honma, and T. Mizusaki, *Phys. Rev. Lett.* **81**, 1588 (1998).
- [6] T. Mizusaki, T. Otsuka, Y. Utsuno, M. Honma, and T. Sebe, *Phys. Rev. C* **59**, R1846 (1999).
- [7] T. Mizusaki, T. Otsuka, M. Honma, and B. A. Brown, *Phys. Rev. C* **63**, 044306 (2001).
- [8] M. Honma, T. Otsuka, B. A. Brown, and T. Mizusaki, *Phys. Rev. C* **65**, 061301 (2002).
- [9] M. Horoi, B. A. Brown, T. Otsuka, M. Honma, and T. Mizusaki, *Phys. Rev. C* **73**, 061305(R) (2006).
- [10] T. Mizusaki, T. Otsuka, M. Honma, and B. A. Brown, *Nucl. Phys. A* **704**, 190c (2002).
- [11] D. Rudolph *et al.*, *Phys. Rev. Lett.* **82**, 3763 (1999).
- [12] E. K. Johansson *et al.*, *Eur. Phys. J. A* **27**, 157 (2006).
- [13] E. K. Johansson *et al.*, *Phys. Rev. C* **77**, 064316 (2008).
- [14] R. R. Betts, B. B. Back, and B. G. Glagola, *Phys. Rev. Lett.* **47**, 23 (1981).
- [15] R. R. Betts, S. B. DiCenzo, and J. F. Petersen, *Phys. Lett. B* **100**, 117 (1981).
- [16] B. K. Dichter, P. D. Parker, S. J. Sanders, R. R. Betts, and S. Saini, *Phys. Rev. C* **35**, 1304 (1987).
- [17] A. Tohsaki-Suzuki and K. Ikeda, *Prog. Theor. Phys.* **69**, 113 (1983).
- [18] J. Zhang, A. C. Merchant, and W. D. M. Rae, *Phys. Rev. C* **49**, 562 (1994).
- [19] J. Darai *et al.*, *Phys. Rev. C* **84**, 024302 (2011).
- [20] E. Uegaki and Y. Abe, *Prog. Theor. Phys.* **127**, 831 (2012).
- [21] E. Uegaki and Y. Abe, *Prog. Theor. Phys.* **127**, 877 (2012).
- [22] R. K. Gupta, S. K. Patra, P. D. Stevenson, C. Beck, and W. Greiner, *J. Phys. G* **35**, 075106 (2008).
- [23] M. Kimura and H. Horiuchi, *Phys. Rev. C* **69**, 051304 (2004).
- [24] T. Ichikawa, Y. Kanada-En'yo, and P. Möller, *Phys. Rev. C* **83**, 054319 (2011).
- [25] Y. Taniguchi, Y. Kanada-En'yo, and M. Kimura, *Phys. Rev. C* **80**, 044316 (2009).
- [26] M. Kimura, R. Yoshida, and M. Isaka, *Prog. Theor. Phys.* **127**, 287 (2012).
- [27] J. F. Berger, M. Girod, and D. Gogny, *Comput. Phys. Commun.* **63**, 365 (1991).
- [28] M. Kimura, *Phys. Rev. C* **69**, 044319 (2004).
- [29] A. S. Reiner, *Nucl. Phys.* **27**, 115 (1961).
- [30] M. Harvey, in *Proceedings of the Second International Conference on Clustering Phenomena in Nuclei, College Park, Maryland, 1975, Report ORO-4856-26* (USEDRA, United States, 1975), p. 549.